ADVANCED MATERIALS
www.advmat.de

3D Printing of Transparent Spinel Ceramics with Transmittance Approaching the Theoretical Limit

Haomin Wang, Li Ying Liu, Pengcheng Ye, Zhangyi Huang, Andrew Yun Ru Ng, Zehui Du, Zhili Dong, Dingyuan Tang, and Chee Lip Gan**

3D printing of transparent ceramics has attracted great attention recently but faces the challenges of low transparency and low printing resolution. Herein, magnesium aluminate spinel transparent ceramics with transmittance reaching 97% of the theoretical limit are successfully fabricated using a stereolithography-based 3D printing method assisted by hot isostatic pressing and the critical factors governing the transparency are revealed. Various transparent spinel lenses and microlattices are printed at a high resolution of ≈100–200 µm. The 3D printed spinel lens demonstrates fairly good optical imaging ability, and the printed spinel diamond microlattices as a transparent photocatalyst support for TiO_2 significantly enhance its photocatalytic efficiency compared with its opaque counterparts. Compared with other 3D printed transparent materials such as silica glass or organic polymers, the printed spinel ceramics have the advantages of broad optical window, high hardness, excellent high-temperature stability, and chemical resistance and therefore, have great potential to be used in various optical lenses/windows and photocatalyst supports for application in harsh environments.

Recently, magnesium aluminate ($MgAl_2O_4$) spinel ceramics have attracted great attention from academia and industry sectors due to its several unique properties, such as ultrahigh transparency at ultraviolet (UV), visible, and infrared (IR) wavelengths (>85% @ λ = 0.25–6.5 µm), excellent mechanical properties, high melting point, low thermal expansion coefficient, and high chemical resistance.[1–3] It has been widely used in various critical optical engineering applications, such as armored or sensor windows, high energy laser windows and sophisticated optical lens. It has replaced some of the traditional transparent single crystals or ceramics (e.g., sapphire, aluminium oxynitride, and zinc sulfide) for applications requiring optical transmission between the wavelengths of ≈2–5 µm. Furthermore, spinel ceramics have very good resistance to radiation induced swelling and strength degradation which makes it a potential insulating material for fusion reactor.[4] The ceramics also have potential to be used as a catalyst or catalyst support for a great variety of reactions including oxidation of sulfur dioxide (SO_2), selective catalytic reduction of nitrogen oxide (NO), n-butane dehydrogenation, and ammonia synthesis, etc.[3,5,6]

Traditionally, spinel ceramics have been fabricated by die pressing, injection molding, or slip casting, followed by a hot press or hot isostatic press (HIP) heat treatment.[1] Ceramics with simple geometries such as flat or curve shapes can be obtained. With the emerging demand for complex shaped spinel ceramics for various applications, such as hyper-hemispherical domes, tangent ogive domes and lenses, there is an urgent need to develop 3D, computer-aided printing of spinel ceramics to ease the design limitations from fabrication.[7–9] The 3D printing technique could further expand its application potential and bring in new design possibility. However, 3D printing of highly transparent spinel ceramics has not been reported yet. Very recently, Pappas et al.[10] have used selective laser melting (SLM) 3D printing method to fabricate magnesium aluminate spinel ceramic, but the samples were translucent with cracks. 3D printing of other transparent ceramics such as Nd:YAG (neodymium-doped yttrium aluminum garnet, $Nd:Y_3Al_5O_{12}$) have also been attempted through direct ink writing (DIW).[11–14] However, the highest transmittance of the ceramics is only ≈70%. Hostaša et al.[15] have fabricated Yb:YAG ceramics plate using stereolithography (SLA) 3D printing method. The transparency of the ceramics achieved is also very low, at only ≈60%. This is because 3D printed ceramics normally contain large amount of structural defects and impurities due to the usage of large volume fraction of organic additives, such as photosensitive resins, dispersants, and plasticizers. In some cases, the volume fraction can be over 50 vol%. When these organic compounds

Dr. H. Wang, L. Y. Liu, Dr. Z. Huang, Prof. Z. Dong, Prof. C. L. Gan
School of Materials Science and Engineering
Nanyang Technological University
Singapore 639798, Singapore
E-mail: clgan@ntu.edu.sg
P. Ye
Creatz3D Pte Ltd.
180 Paya Lebar Road, Singapore 409032, Singapore
Dr. A. Y. R. Ng, Dr. Z. Du, Prof. C. L. Gan
Temasek Laboratories
Nanyang Technological University
Singapore 637553, Singapore
E-mail: duzehui@ntu.edu.sg
Prof. D. Tang
School of Electrical and Electronic Engineering
Nanyang Technological University
Singapore 639798, Singapore
The ORCID identification number(s) for the author(s) of this article can be found under https://doi.org/10.1002/adma.202007072.

DOI: 10.1002/adma.202007072

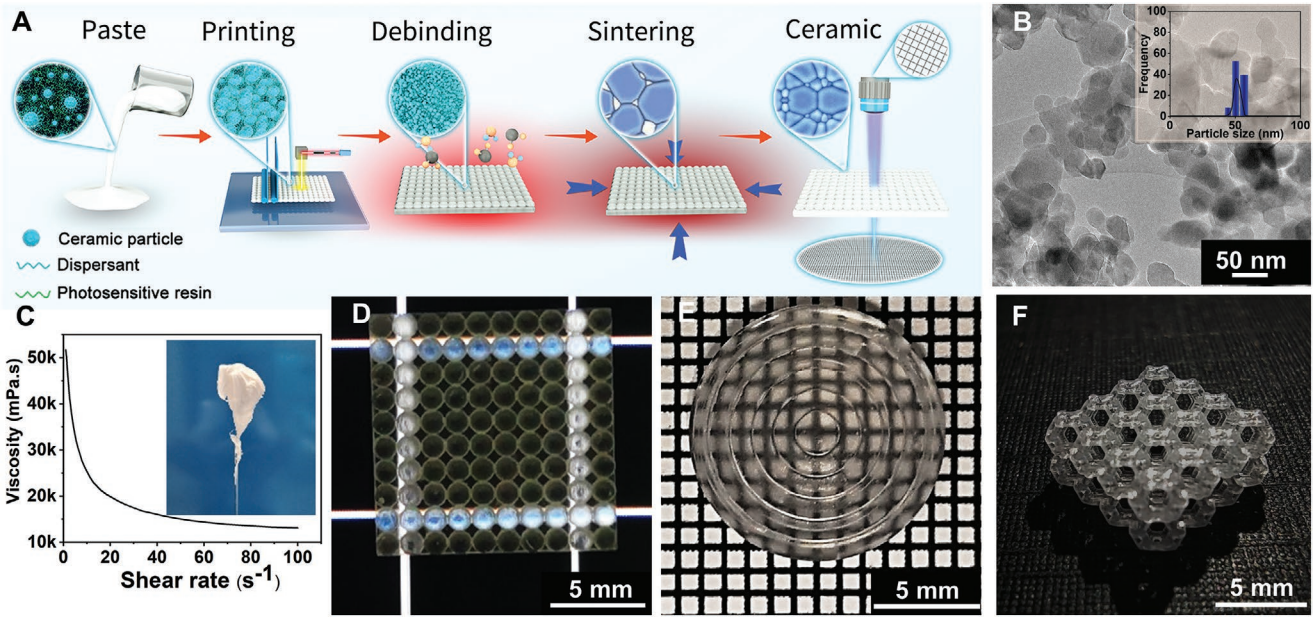

Figure 1. A) Schematic illustration of the 3D printing and post heat treatment process of spinel ceramics. B) TEM image of spinel nanoparticles and particle size distribution (inset). C) The rheological behavior of printable spinel ceramic paste with 55 wt% solid load and 3 wt% dispersant, inset showing the photo of spinel ceramic paste with good self-holding ability. D–F) Photos of printed spinel transparent prototypes: lens array (D), Fresnel lens (E), Kelvin cell microlattice (F).

decompose, they leave behind many nano- or micropores in the grain boundaries and within grains. Some impurity phases may also be present. These defects can significantly degrade the transparency of ceramics. Another reason for the opaqueness of ceramics can be attributed to its polycrystalline nature as the grain boundaries can induce scattering. Therefore, 3D printing of transparent ceramics is much more challenging compared with printing of transparent fused silica glass.[16]

Herein, we describe a SLA 3D printing method assisted by HIPing to fabricate highly transparent $MgAl_2O_4$ spinel ceramics with high printing resolution. Three strategies have been adopted to enhance the transparency of the ceramics, namely: 1) using ultrafine and ultrapure spinel nanoparticles with a mean diameter of 50 nm to prepare the printable paste; 2) using a multi-step debinding process with controlled atmosphere to thoroughly remove the organic additives in the ceramic green bodies; and 3) optimizing the HIPing process to completely remove micro- or nanopores induced by the decomposition of the organic additives. As the particle size of the spinel powders used is far smaller than the wavelength of the UV light used for curing in the SLA printing process (355 nm), scattering of UV light by the spinel particles is significantly reduced. This leads to a very high printing resolution of ≈100–200 µm, which is much higher than that of many 3D printed ceramics reported so far.[8,11,13,17,18] The multi-step debinding and HIPing process used in this work produced spinel ceramics with transparency approaching the theoretical limit. Therefore, our modified 3D printing and post heat-treatment processes pave a way to fabricate spinel ceramics with high transparency and complex shapes with very fine feature size. As a demonstration of the potential applications of the printed spinel ceramics, various transparent optical components such as lens array, Fresnel lens, hemispherical dome, and microlattices (e.g., Kelvin cell, simple cubic) have been printed and some have been tested on their optical imaging ability. The 3D printed spinel gyroid and diamond microlattices have been tested as transparent support to immobilize TiO_2 photocatalyst on their sheet surfaces and their effect on the photocatalytic efficiency have been investigated.

Figure 1A schematically illustrates the 3D printing and post heat-treatment process of spinel ceramics. Highly pure spinel ceramic nano powders were first dispersed in photosensitive resin trimethylolpropane triacrylate (TMPTA) with the assistance of a dispersant (Solsperse 85000, Lubrizol) to prepare a printable ceramic paste. The morphology and size distribution of the spinel powders are shown in Figure 1B. The particles have a very narrow size distribution, ranging between 40–60 nm and averaging at ≈50 nm. The ceramic paste exhibits a significant shear-thinning behavior, with a viscosity of ≈12.8 Pa s at a shear rate of 30 s^{-1} (Figure 1C). Inset of Figure 1C shows a photo of the paste, demonstrating excellent self-holding ability which is important for the as-printed components to retain their shapes without any additional support. The ceramic paste was printed by a commercial SLA 3D printer (Ceramaker C900FLEX, 3DCeram). The printed ceramic green bodies have very smooth surfaces, with surface roughness of only ≈31 nm (Figure S1, Supporting Information) because spinel nanopowders were used in the paste.

After printing, the ceramic green body was debinded in multiple steps in which the temperature ramping-up and dwelling steps were conducted in N_2 atmosphere to slow down the decomposition process and finally in air to completely remove the organic additives. Lastly, highly transparent spinel ceramics were obtained after a two-step sintering process, that is, pressureless pre-sintering and then HIPing. Figure 1D–F shows the 3D printed and HIPed highly transparent spinel lens array, Fresnel lens and Kelvin cell microlattice. Hemispherical

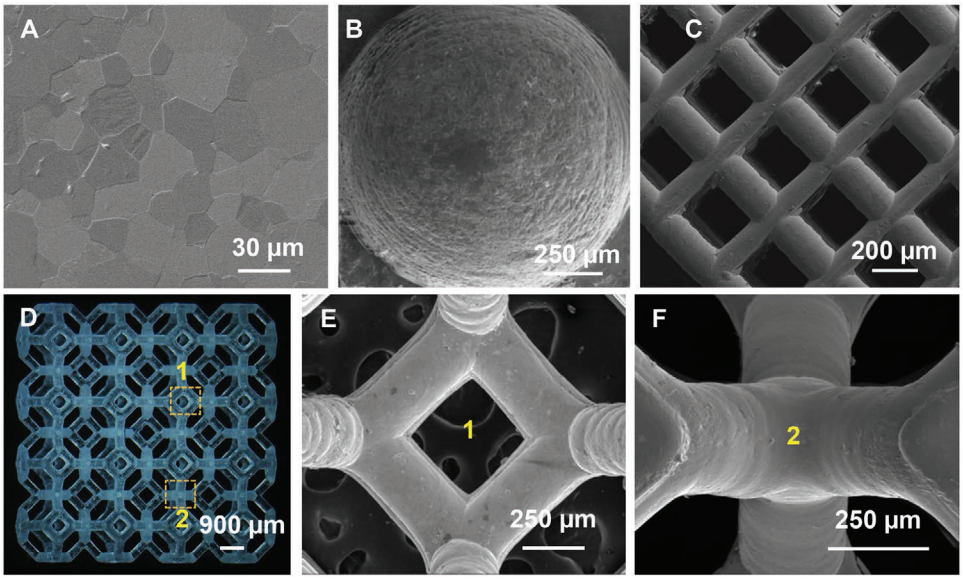

Figure 2. A) SEM image of a spinel ceramic surface after polishing and thermal etching. B,C) SEM images of one lens in the printed lens array shown in Figure 1D (B), and a simple cubic microlattice (C). D) Optical image of the Kelvin cell microlattice. E,F) SEM images of the struts zoomed-in from Zone #1 and #2 in (D), which represent the struts in horizontal plane (i.e., paste-cast planes) and in the planes tilted from the paste-cast planes. All the samples have been HIPed to fully dense.

dome and simple cubic microlattice have also been fabricated and shown in Figure S2 in the Supporting Information. The lens and microlattices were printed according to the 3D digital models designed by SolidWorks software and shown in Figures S2 and S3 in the Supporting Information. The topology and dimensions of the printed objects resemble the original design very well. The measured relative density of the ceramics after HIPing process reached 99.9% (the theoretical density of spinel ceramic is 3.65 g cm^{-3}). **Figure 2**A shows the microstructure of the ceramics after polishing and thermal etching. The ceramics have very dense, almost pore-free grain packing and the average grain size is ≈19 μm. Such medium grain size enables the ceramics to exhibit high optical quality and good mechanical strength at the same time.

Figure 2B shows the magnified image of one lens in the lens array after HIPing. The spinel convex lens array was designed to have a focal length of 0.89 mm at the wavelength of 632 nm (visible light) or 1 mm at the wavelength of 4 μm (infrared light) and the aperture diameter is 1.27 mm. The actual diameter of the fabricated lens measured from the scanning electron microscopy (SEM) images is ≈1.3 mm, which is ≈30 μm (or ≈2.4%) larger than the designed diameter. Based on the actual aperture diameter, the focal length of the printed lens at λ = 632 nm is ≈0.91 mm, with a very small deviation of ≈20 μm (or ≈2.4%) from the designed value. These results are very encouraging as it indicates that various optical lens can be realized with high size accuracy through SLA 3D printing of spinel transparent ceramics. The SEM image in Figure 2B shows that the top surface of the printed spinel lens is comparatively smooth, while the lateral surface near to the bottom is very rough, with a stripe-like appearance which is induced by the layer-by-layer printing manner used in the work.

Figure 2C is an SEM image of the sintered simple cubic microlattice zoomed in from Figure S2D, Supporting Information. The diameter of the thin and thick struts is ≈ 115 and ≈168 μm, respectively and the strut length is 500 μm. Figure 2D–F is the image of the Kelvin cell microlattice sample. The strut diameter is ≈220 μm and the length is ≈600 μm. The surface of the struts aligned in the spinel paste-cast plane is very smooth (Figure 2E). However, the lateral sides of the struts tilted from the paste-cast plane are rough (Figure 2F), similar to that observed in the printed lens. This, again, can be attributed to the layer-by-layer printing manner and the thick cast layers (≈30 μm in this work) worsen the surface finish. If the cast layer can be as thin as ≈1 μm, sub-micrometer surface roughness can be obtained, which, however, is still a technical challenge for commercially available ceramic SLA 3D printer. Nevertheless, it is noteworthy that the feature printing resolution of the 3D printed spinel ceramics can be as small as ≈115–220 μm, as evidenced by the printed Kelvin cell and simple cubic lattices. It is possible to further push the printing resolution to below 100 μm as the line cured by one laser scan across the paste is ≈70 μm in size (Figure S4, Supporting Information). However, the printing resolution is limited by the paste casting manner used to build the 3D green body. If the strut is too thin, e.g., <100 μm, it may be damaged by the blade when it sweeps new paste over it to create new layers. Nevertheless, the printing resolution of ≈100–200 μm is much smaller than that of other 3D printing techniques of ceramics (typically ≈0.5–1 mm),[10–15,18] and is still unachievable by conventional ceramic shaping and machining technique.[1,3,19]

In order to obtain highly transparent spinel ceramics, a critical controlling factor is the uniformity of the green body density. No large pores or agglomerates are allowed to be formed in the green bodies. Dispersion of the spinel nanopowders in the acrylate resins has great influence on the powder packing density of the green bodies. **Figure 3**A–C shows the sedimentation test result of a spinel suspension with 0.5 wt% dispersant

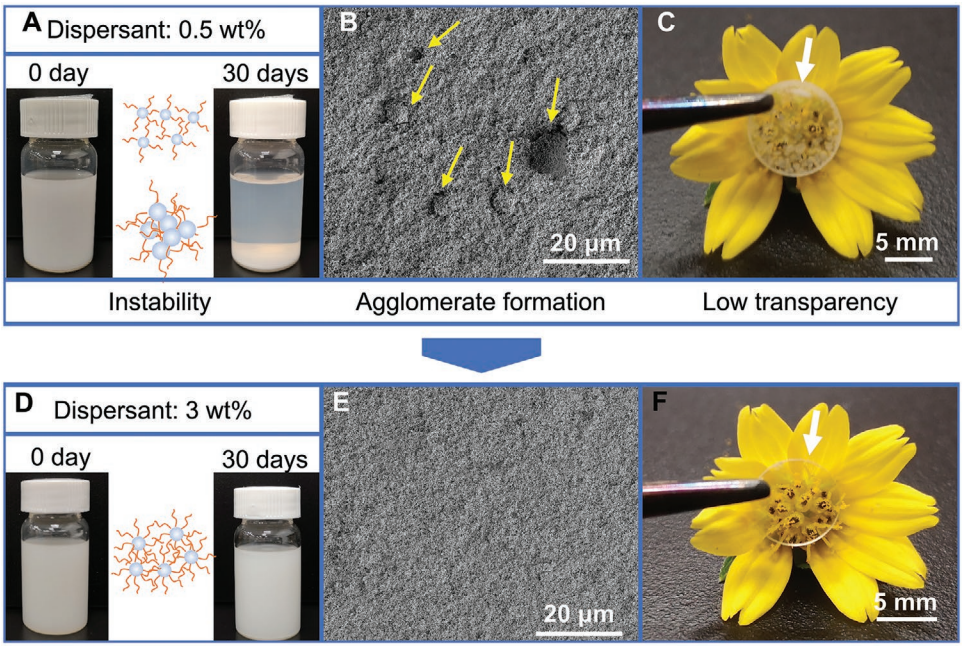

Figure 3. A) Sedimentation test result of 10 wt% spinel ceramic powders suspension with 0.5 wt% dispersant, showing that this suspension is not stable. B) SEM image of the spinel green body printed from the paste with 55 wt% spinel powder and 0.5 wt% dispersant, and C) photo of the resultant sintered ceramics, indicated by the white arrow. D) Sedimentation test result of 10 wt% spinel ceramic powder suspension with 3 wt% dispersant. E) SEM image of the spinel green body printed from the paste with 55 wt% spinel powder and 3 wt% dispersant and F) the resultant sintered ceramics, indicated by the white arrow.

(weight percentage to powder weight), an SEM image of the resultant green body and a photo of the sintered ceramics, respectively. As the dispersant used for dispersing the spinel powders in the acrylate resin was not sufficient (only 0.5 wt%), the repulsive energy of the powder surfaces was low, which resulted in coagulation of the powders and thus precipitation of large agglomerates in the suspensions. Many agglomerates and large pores were formed in the printed spinel green body, as shown in Figure 3B (pointed by arrows). It is very difficult to remove such microscale pores by sintering, even with high pressure assistance. The sintered sample is seen to have many white spots or becomes whitish (Figure 3C).

Figure 3D shows the sedimentation test result of a spinel suspension with 3.0 wt% dispersant. The suspension remained stable after settling for 30 days. This indicates that the colloidal particles in the solution have reached a balance in the interparticle attraction–repulsion force. Nanoparticle coagulation has been eliminated by a large extent. Therefore, the spinel green body printed from the paste with 3 wt% dispersant and 55 wt% ceramic powder has very uniform and dense powder packing, with the voids between powders in nano size range (Figure 3E). Thus, the resultant spinel ceramic after HIPing exhibits crystal-clear transparency (Figure 3F).

A thermal debinding process is another important step to control the uniformity in the chemical composition and the density of green bodies as the printed spinel green bodies have a large amount of organic additives (≈45 wt%). A non-optimized debinding process can result in carbon residuals, pores and even cracks in the green bodies, as shown in Figure S5A,B (Supporting Information). Through systematic studies on the effect of debinding process parameters, an optimized debinding process was designed with slow heating/cooling rate of 0.5 °C min^{-1} and multiple steps of dwelling at the temperatures where majority of decomposition occurs, as shown in Figure S5C (Supporting Information). Crack-free samples have been obtained after debinding (Figure S5D, Supporting Information).

Pre-sintering and HIPing are the most critical but challenging steps to get highly transparent spinel ceramics as the sintering window of spinel ceramics is very narrow. The pre-sintering step was conducted in a normal box furnace to enhance the density of spinel green bodies to over 90% relative density and no open pores remained. **Figure 4**A–C shows the fracture surfaces of the spinel ceramics pre-sintered at 1600–1700 °C for 20 h. Intergranular open pores seen in the 1600 °C pre-sintered samples have been mostly removed at the sintering temperature of 1650 °C and the relative density of the ceramic reaches ≈95%. When the pre-sintering temperature was increased by another 50 °C (i.e., 1700 °C), abnormal grain growth occurred, which caused many pores to be trapped inside the grains. Once these intragranular pores are formed, it is very difficult to remove them even with high temperature and/or high pressure.[20] The samples remain opaque after pre-sintering (Insets of Figure 4A–C). Therefore, the pre-sintering temperature should be kept in a very small range of around 1650 °C.

HIPing temperature was studied in the range of 1700–1800 °C with gas pressure fixed at 180 MPa and dwelling time of 15 h. All of the samples were pre-sintered at 1650 °C. Figure 4D–F shows the fracture surfaces of the ceramics. Most pores were removed from the ceramic matrix at the HIPing temperature of 1750 °C and pore-free ceramics have been obtained at 1800 °C. The HIPing temperature of 1800 °C for full densification of the

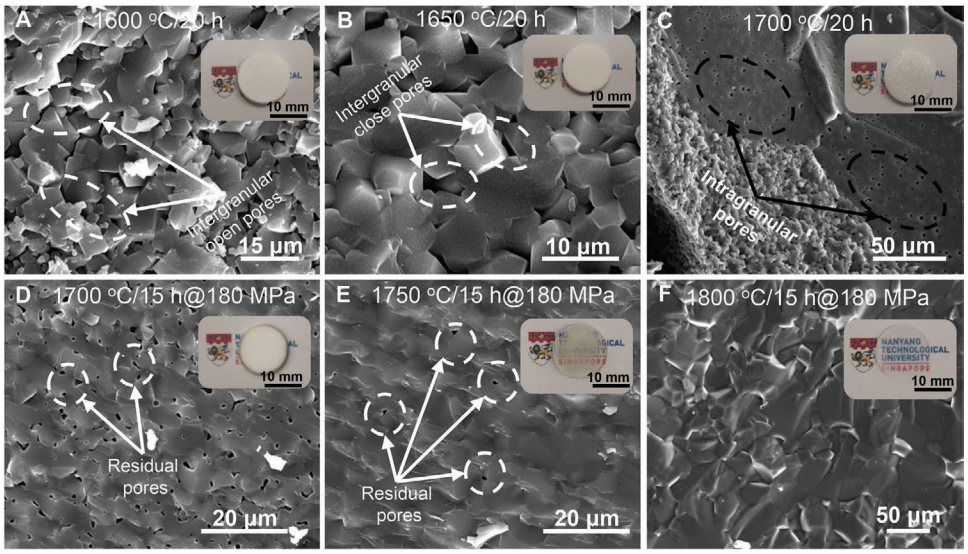

Figure 4. A–F) SEM images of the fracture surfaces of the printed spinel ceramics pre-sintered at different temperatures (1600, 1650, and 1700 °C) (A–C) and HIPed at different temperatures (1700, 1750, 1800 °C) after pre-sintering at 1650 °C (D–F). The insets of (A–F) are photos of the corresponding spinel ceramics.

printed spinel is comparable to 1700–1850 °C reported in literatures for densifying the spinel ceramics with the assistance of sintering aids (e.g., SiO_2, LiF, and CaO).[1] This implies that the spinel nanopowders used in this work have a very high sintering activity. The spinel ceramics evolve from being opaque to transparent as the HIPing temperature increases, as shown in the insets of Figure 4D–F. Highly transparent ceramics can be obtained with HIPing temperature of 1800 °C. The result reveals that the HIPing process is a crucial and effective step to densify the spinel ceramics, especially for 3D printed spinel ceramics of which, a large volume of pores is present in the green bodies. It is worth mentioning that the sintering shrinkage rate of the ceramics after HIPing is 38.3% in height and 34.7% in diameter. These shrinkage rates are lower than that of the printed silica glass (i.e., ≈50%)[16,21] and help to reduce the geometrical deviation between the printed and the designed structures for intended applications.

Figure 5A shows the transmission spectrum of the spinel ceramic disk with a thickness of 1.2 mm made by the optimized 3D printing, debinding, and HIPing processes. The sample exhibits a maximum transmittance of ≈84.8% at the wavelength of 1550 nm. The theoretical limit (T_t) of the transmittance of spinel ceramics can be calculated by:[22]

$$T_t = 2n/(n^2+1) \tag{1}$$

where n is the refractive index which is a function of wavelength λ:[23]

$$n^2 - 1 = \frac{1.8938\lambda^2}{\lambda^2 - 0.09942^2} + \frac{3.0755\lambda^2}{\lambda^2 - 15.826^2} \tag{2}$$

The theoretical transmittance limit at λ = 1550 nm is ≈87%. Therefore, the 3D printed spinel ceramics have a transmittance reaching ≈97% of the theoretic limit at the wavelength of 1550 nm. The transmittance is comparable to or even better than that of the spinel ceramics made by conventional dry press method followed by HIPing process (75–85%).[1,2] The ultrahigh transparency of the ceramics can be attributed to the uniform and dense microstructure of the ceramics shown in Figure 2A.

Figure 5B presents the Vickers hardness of the 3D printed spinel ceramics, together with the hardness data of dry pressed spinel ceramics, silica glass, polycarbonate (PC), and poly(methyl methacrylate) (PMMA) polymers. The Vickers hardness of our 3D printed spinel ceramics averages at ≈13.5 ± 0.4 GPa. The values are comparable to that of those spinel ceramics made by conventional dry press method (≈12–15 GPa).[1] Silica glass, PC, and PMMA are commonly-used transparent materials that have been successfully 3D printed for optical applications.[24] Their hardness values are ≈11, 0.4, and 0.2 GPa, respectively.[25,26] Comparatively, the 3D printed spinel ceramics are much harder. Moreover, the spinel ceramics can retain high transparency even when being heated at 800–1100 °C by a Bunsen burner, as shown in Figure 5C (sample indicated by the arrow). The sample remained intact after cooling. PC and PMMA cannot withstand such high temperature and they will either soften or be burned off. Therefore, the 3D printed spinel ceramics have great potential to be used in various optical windows and lens for harsh environment as the ceramics combine a few advantages, such as high transparency, high hardness, and high-temperature stability. The design flexibility offered by 3D printing further broadens their application fields.

Figure 6 is a comparison of the 3D printed spinel ceramics with other printed transparent ceramics (i.e., YAG) and glass reported so far, in terms of maximum relative transmittance and printing resolution. Here, the maximum relative transmittance (T_{rm}) is a ratio of the highest measured transmittance (T_{em}) to the theoretical transmittance limit (T_t) calculated by Equation (1) at the same wavelength, as shown in the following relationship:

$$T_{rm} = \frac{T_{em}(\lambda_m)}{T_t(\lambda_m)} \tag{3}$$

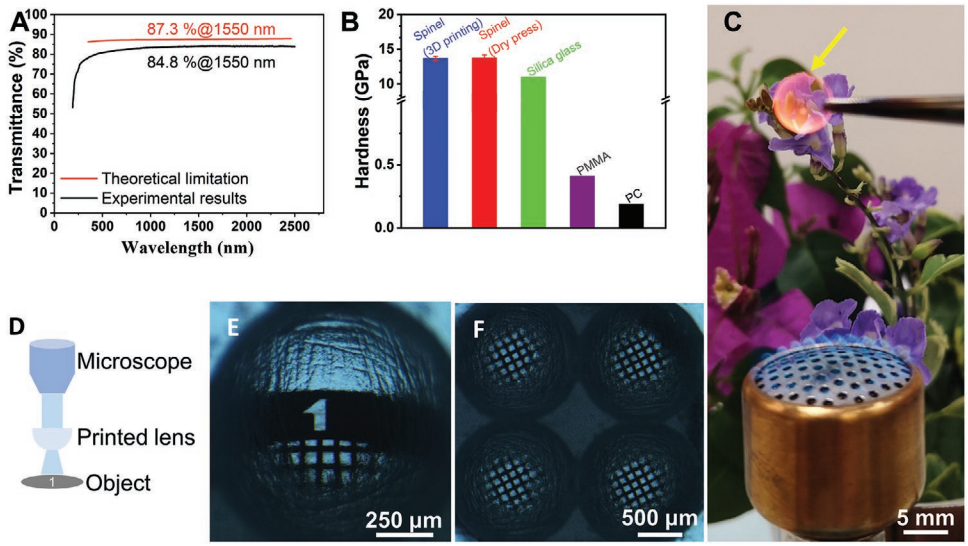

Figure 5. A) Transmission spectrum of the printed and HIPed spinel ceramics with a thickness of 1.2 mm, together with the theoretical transmittance limit calculated by $T_t = 2n/(n^2 + 1)$. B) Microhardness of the HIPed spinel ceramics, together with the data of spinel ceramics made by dry pressing, the silica glass, PC, and PMMA polymers.[25,26] C) Photo showing the spinel ceramic under heating at 800–1100°C by a Bunsen burner. D) A schematic illustration of the optical imaging setup and E,F) images of Arabic numeral "1" (E) and microgrid (F) projected from the 3D printed spinel ceramic lens array shown in the setup in (D).

where λ_m is the wavelength corresponding to the measured maximum transmittance. The printing resolution is defined as the finest strut diameter or width of a printed object that a printing technique can produce. Fused silica glass has been intensively studied for various printing techniques, such as SLA, DLP, DIW, SLS, and FDM method.[16,21,27–33] Here, DLP and SLS refer to Digital Light Processing and the selective laser sintering technique, respectively. FDM is a fused deposition modelling technique. The highest measured transmittance of printed glass reported so far is in the range of ≈80–90% at the visible and near infrared wavelengths from 300 to 1100 nm, which corresponds to the maximum relative transmittance of ≈80–96%. The printing resolution of the SLS, FDM, and DIW techniques for fused silica glass is rather low, varying in ≈0.6–5 mm, while the printing resolution of SLA and DLP can reach ≈80–200 µm. YAG ceramics have been printed by DIW, SLA, and DLP method, but it is not well studied yet.[11–13,15] The DIW printed YAG ceramics have maximum relative transmittance of ≈83–94%, but the printing resolution is very low, only ≈ 0.5–1 mm. The SLA printed YAG ceramics have shown better printing resolution of ≈100 µm, however, the highest measured transmittance is ≈60% (at 2520 nm wavelength), only reaching 71% of theoretical transmittance limit (T_t = 84.2%). There is still a large gap between the measured transmittance and the transmittance requirement for optical application.

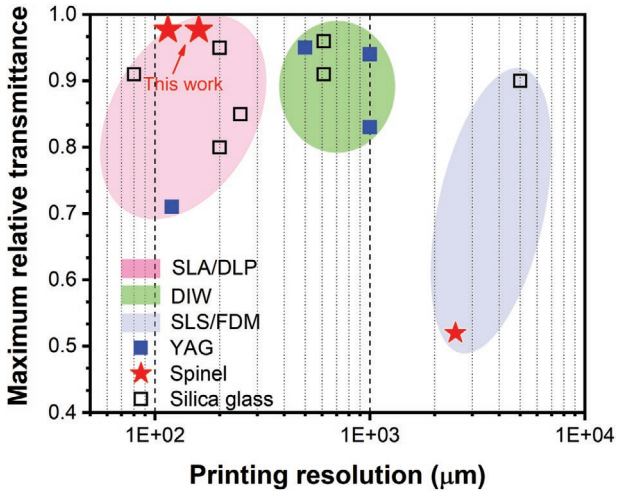

Figure 6. Plot of the maximum relative transmittance against printing resolution of the 3D printed transparent spinel ceramics in this work, together with the data of other printed transparent ceramics (YAG)[11–31] and glasses for comparison.[16,21,29–32]

In our work, we have successfully 3D printed complex shaped spinel ceramics with a printing resolution as small as ≈100–200 µm and the measured transmittance of 84.8% which corresponds to ≈97% of the theoretical transmittance limit. The optical quality of the spinel ceramics is closest to the theoretical transmittance limit, compared with the printed silica glass and YAG ceramics.[11–13,15,16,21,28–33] The printing resolution is much higher than that of many other printed transparent materials. Therefore, our work has simultaneously circumvented the two bottlenecks in optical transparency and printing resolution of the state-of-the-art 3D printing techniques of transparent ceramics and glass, thus enabling the harnessing of the advantages of the unique physical properties of spinel ceramics and the flexibility of SLA 3D printing technique to create various advanced spinel based optics and catalyst supports for engineering applications.

As a demonstration on the application of the 3D printed spinel ceramics, the optical imaging performance of the spinel convex lens array shown in Figure 1D was characterized by an optical microscopy system schematically depicted in Figure 5D.

The spinel convex lens was placed between the objective lens of the microscope and the object, such as an Arabic numeral "1" and a transmission electron microscopy (TEM) Cu grid. Images of the Arabic numeral "1" and the microgrids can be clearly observed through the spinel lens without distortion, as shown in Figure 5E,F. The images of the microgrids viewed from four different spinel lenses have equally clear quality with high contrast and sharpness. These demonstrations indicate the great potential of the 3D printed spinel ceramics in the application of various optical lens, windows, and artificial compound eyes for cutting-edge applications in robotics, medical endoscopes, surveillance devices, and reconnaissance systems.

The printed transparent spinel ceramics can also be used as a catalyst support to immobilize various photocatalyst for the applications of water treatment, water splitting, ammonia synthesis, and solar energy conversion, etc.[34–38] In a conventional photocatalytic reactor, photocatalysts such as TiO_2 are usually immobilized on support materials such as glass, stainless steel, alumina, activated carbon, zeolite, and silica gel to avoid a tedious post separation process and facilitate the recycling of the photocatalyst.[39–44] Compared with these conventional support materials, 3D printed transparent spinel ceramics can have larger illuminated surface area, low light absorption, and can delicately control the mass flow by rational design of the hollow channels inside the ceramics and therefore offer much higher photocatalytic efficiency. **Figure 7**A schematically illustrates a photocatalytic reactor with the printed spinel ceramic lattices as a support to immobilize TiO_2 photocatalyst for water treatment and its working mechanism. In this work, a few types of photocatalyst supports consisting of the spinel diamond and gyroid sheet-based microlattices have been prepared and tested for benchmarking their resultant photocatalytic efficiency. The diamond and gyroid microlattices are with solid volume fraction (V_f) of 0.35 and surface areas of ≈1767 and ≈1569 mm^2 (for sample size: ≈6.3 mm × 6.3 mm × 18.9 mm), respectively. Figure 7B,C show the photocatalyst supports assembled with the two types of the printed transparent spinel microlattices and coated with TiO_2 thin films. Photocatalyst supports using opaque spinel ceramic lattices of same dimensions have also been prepared for comparison which have the same volume fraction of 0.35 but slightly larger surface areas of ≈1779 and ≈1699 mm^2 for diamond and gyroid lattices, respectively. SEM and energy-dispersive X-ray spectroscopy (EDX) mapping images of the samples in Figure 7D,E and Figure S6A–C (Supporting Information) confirm that the TiO_2 coating was present uniformly on the spinel sheet surface. The thickness of the TiO_2 films is ≈ 600 nm (refer to Figure S6D, Supporting Information). In the photocatalytic activity test, a common water pollutant, methyl orange with a concentration of 2.5 mg L^{-1} in water was used and it was found to be decolored after exposing to UV light for 1 h in the presence of the TiO_2 coated transparent spinel photocatalyst support. The kinetic photodegradation test results are

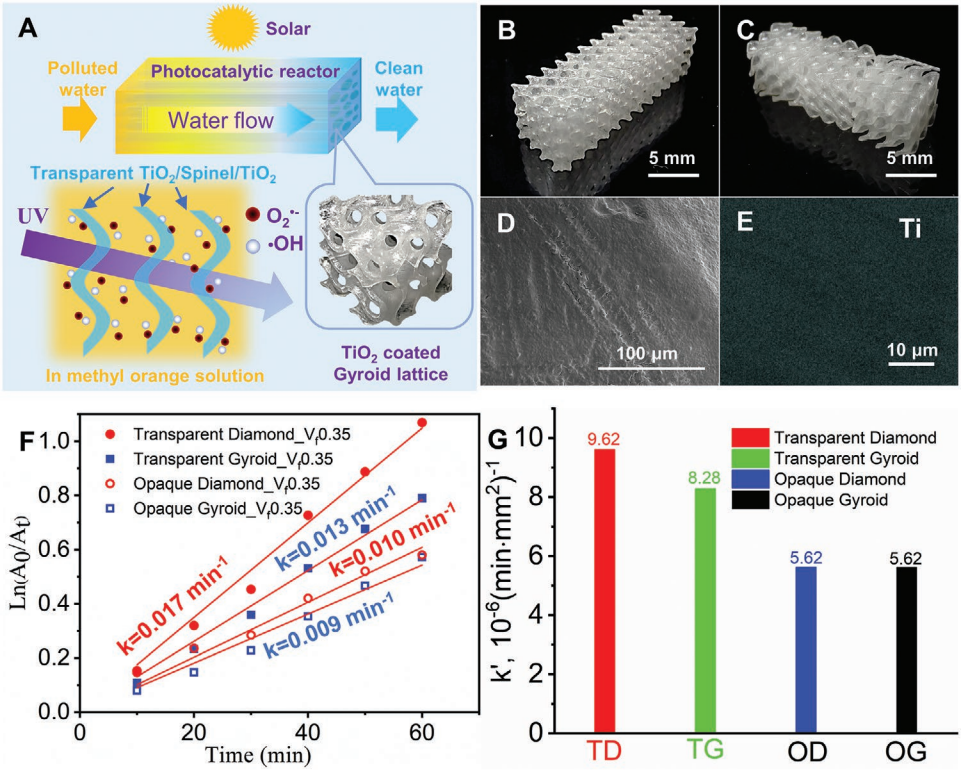

Figure 7. A) Schematic illustration of a photocatalytic reactor using the printed transparent spinel as photocatalyst support for water treatment. B,C) Photographs of two types of spinel photocatalyst support coated with TiO_2 and designed as diamond (B) and gyroid (C) lattice structure. D) Microstructure and E) EDX mapping (Ti) of TiO_2 films coated on the sheet surface of the printed spinel lattices. F) Plot of $\ln(A_0/A_t)$ versus irradiation time (t) and G) Bar chart of the normalized rate constant (k') of the different types of spinel photocatalyst support (TD: transparent diamond; TG: transparent gyroid; OD: opaque diamond; OG: opaque gyroid).

shown in Figure 7F. The photocatalytic decolorization of methyl orange solution can be described as follows:

$$\ln\left(\frac{A_0}{A_t}\right) = kt \tag{4}$$

where A_t and A_0 are the absorption peak of the methyl orange solution after UV irradiation for a period of t (min) and on original condition, respectively. k is the apparent reaction rate constant. By linearly fitting the data of $\ln(A_0/A_t)$ versus t in Figure 7F, the reaction rate constant of the TiO_2 films immobilized by the spinel microlattices can be obtained. The TiO_2 films coated on the opaque gyroid and diamond lattices has a very low reaction rate constant, only 0.009 and 0.010 min^{-1}, respectively. The highest reaction rate constant of 0.017 min^{-1} is found on the transparent TiO_2-coated diamond microlattices. The transparent TiO_2-coated gyroid lattices has slightly lower reaction rate constant of 0.013 min^{-1} due to its smaller surface area compared with diamond lattices. Figure 6G benchmarks the photocatalytic efficiency of the TiO_2 films coated on the 4 types of photocatalyst supports and the data of the reaction rate constant have been normalized by the total surface area of the spinel microlattices for a fair comparison. The transparent diamond microlattices still have the highest value of 9.62×10^{-6} $(min\ mm^2)^{-1}$, followed by the transparent gyroid microlattice (8.28×10^{-6} $(min\ mm^2)^{-1}$). This is likely because the diamond microlattices have smaller hollow channels inside the unit cell and therefore the length of the path for the dye molecules to diffuse from the solution to the catalyst surface is shorter, resulting in faster photodegradation. The opaque gyroid and diamond lattices show similarly low normalized reaction rate constant (k') of 5.62×10^{-6} $(min\ mm^2)^{-1}$ as mainly the top surface of these spinel lattices are exposed to the UV light, while the other surfaces are blocked due to their opaqueness. Therefore, the transparent spinel support results in much higher photocatalytic efficiency. Furthermore, the photocatalytic efficiency can be further improved by tailoring the surface area and geometry of the open channels inside the ceramic lattices.

In summary, magnesium aluminate spinel transparent ceramics with transmittance reaching 97% of the theoretical limit have been successfully fabricated by SLA 3D printing method assisted by HIPing and a printing resolution as high as ≈100–200 µm is obtained. The ceramics have microhardness of ≈13.5 GPa and can retain its transparency at the temperature of 800–1100 °C. The critical factors governing the transparency of the printed spinel ceramics have been revealed, including suitable dispersant concentration (3 wt%), debinding profile and sintering temperatures. The temperature window of pre-sintering of the ceramics is ≈1650 °C and the HIPing temperature for full densification of the ceramics is 1800 °C.

The printed spinel convex lens array has shown fairly good optical imaging capability and the printed spinel diamond microlattices as a transparent photocatalyst support for TiO_2 have significantly enhanced its photocatalytic efficiency compared with opaque counterparts and the transparent gyroid lattice which has a smaller free surface area. Therefore, 3D printed spinel ceramics have great potential to be used in various optical windows and lens, and support materials for photocatalysts.

Experimental Section

Materials: Commercial spinel nanopowders (S30CR) with a specific surface area of 28 $m^2\ g^{-1}$ from Baikowski were used as raw material. The particle size of the powders was characterized by TEM (JEOL2010). The particle size distribution was measured using the dynamic light scattering method (SZ100, HORIBA, Japan). Photosensitive trimethylolpropane triacrylate (TMPTA) resin, photoinitiator 2-hydroxy-2-methylpropiophenone (PI) and methyl orange were bought from Sigma-Aldrich. Solsperse 85000 from Lubrizol was used as dispersant.

Printing of the Spinel Green Bodies: The printable spinel ceramic pastes have been prepared by mixing the ceramic powders (55 wt%), dispersant (0.5–3.0 wt%), PI (0.3 wt%), and TMPTA (remaining) using vacuum planetary mixer (AVR310, Thinky, Japan). Sedimentation tests have been conducted on the spinel suspensions with 10 wt% solid load and different concentrations of dispersant to determine the optimal dispersant concentration.

Before printing, 3D digital models of convex lens array, Fresnel lens, hemispherical dome, Kelvin cell, simple cubic, gyroid, and diamond microlattices were designed using commercial software of SolidWorks and shown in Figures S2 and S3, Supporting Information. The spinel green bodies were printed according to these 3D digital models by a commercial SLA 3D printer (Ceramaker C900 FLEX, 3DCeram) which is equipped with a UV laser with beam diameter of 50 µm and wavelength of 355 nm. The printing is a casting/photocuring alternating process with a blade sweeping new paste across the cured layer beneath to control each layer thickness (≈30 µm in this work). The cast layer was then selectively cured by exposing to the UV laser. Through the layer-by-layer casting/curing process, the spinel 3D green bodies were printed.

Debinding/Sintering Process: In order to remove the organic additives in the printed ceramic green bodies, the multiple-step debinding process was conducted in a tube furnace (GHA 12/450, Carb Lite Gero). The debinding process consisted of multiple steps of heating in nitrogen and then in air and the heating/cooling rate was fixed at 0.1–1.0 °C min^{-1}. The multi-step dwelling temperatures include: 250, 350, 450, and 600 °C and the dwelling time at each step is ≈5 h.

After debinding, the ceramic green bodies were pre-sintered in a box furnace (LHT 04/18, Nabertherm) at 1600–1700 °C for 25 h and then treated with HIP (AIP10-30H, AIP) process at 1700–1800 °C for 15 h under 180 MPa Ar gas pressure.

Characterization: The surface roughness of the as-printed spinel green body was measured by Surface Profiler (ASIQ, KLA Tencor). The transmittance of the printed and sintered ceramics was measured using UV–vis–NIR spectrometer (Cary 5000 UV–vis, Agilent). Sample surfaces were carefully polished with diamond paste before the measurement. Microhardness of the spinel ceramics was measured according to ASTM C1372-15 using 4.9 N load and dwelling time of 15 s. The morphology of the printed ceramic objects and the microstructure of the ceramics have been studied by SEM (Nova 600i, FEI). The optical imaging performance of the printed convex lens array was characterized on an optical microscope equipped with a CCD camera (SZX16, OLYMPUS).

Photocatalytic Activity Test: TiO_2 thin films were coated on the transparent spinel diamond and gyroid lattice as a support by sol–gel dip coating process[45] followed by annealing at 500 °C for 1 h. Opaque spinel photocatalyst supports were also prepared through the same processing route but without post HIPing process for comparison. The compositions of the thin films were analyzed by energy-dispersive X-ray spectroscopy (EDX). In the photocatalytic activity test, the TiO_2 coated photocatalytic support with size of ≈6.3mm × 6.3mm × 18.9 mm were put in aqueous methyl orange solution with a concentration of 2.5 mg L^{-1} in a quartz cell (10mm × 10mm × 30mm). A UV lamp (F500, Incure) with light intensity of 435 mW cm^{-2} was used as light source. The photodegradation kinetics of the methyl orange were studied by measuring the light absorbance of the methyl orange using UV–vis–NIR spectrometer (Cary 5000 UV–vis, Agilent) after exposure to UV light for different time intervals.

Supporting Information

Supporting Information is available from the Wiley Online Library or from the author.

Acknowledgements

The authors would like to acknowledge with thanks the financial support of the work by A*STAR AME IRG grant with project number of A1883c0009. H.W. would like to thank Dr. Yuezhong Wang for discussion. Z.D. would like to thank Dr. Lai Wenn Jing and Mr. Sean Looi for insightful discussion and thanks Yida Zhao and Dr. Zhang Hao for drawing the 3D lattice model and some of the SEM analysis.

Conflict of Interest

The authors declare no conflict of interest.

Data Availability Statement

The data that support the findings of this study are available from the corresponding author upon reasonable request.

Keywords

optical imaging, photocatalyst support, spinel, stereolithography (SLA), transmittance

Received: October 16, 2020
Revised: January 22, 2021
Published online:

[1] M. Rubat du Merac, H.-J. Kleebe, M. M. Müller, I. E. Reimanis, *J. Am. Ceram. Soc.* **2013**, *96*, 3341.
[2] Z. Xiao, S. Yu, Y. Li, S. Ruan, L. B. Kong, Q. Huang, Z. Huang, K. Zhou, H. Su, Z. Yao, W. Que, Y. Liu, T. Zhang, J. Wang, P. Liu, D. Shen, M. Allix, J. Zhang, D. Tang, *Mater. Sci. Eng.: R Rep.* **2020**, *139*, 100518.
[3] I. Ganesh, *Int. Mater. Rev.* **2013**, *58*, 63.
[4] S. Sharafat, N. M. Ghoniem, P. I. H. Cooke, R. C. Martin, F. Najmabadi, K. R. Schultz, C. P. C. Wong, *Fusion Eng. Des.* **1993**, *23*, 99.
[5] B. Srikanth, R. Goutham, R. Badri Narayan, A. Ramprasath, K. P. Goimath, A. R. Sankaranarayanan, *J. Environ. Manage.* **2017**, *200*, 60.
[6] M. A. Mohd Adnan, N. Muhd Julkapli, M. N. I. Amir, A. Maamor, *Int. J. Environ. Sci. Technol.* **2019**, *16*, 547.
[7] Z. Chen, Z. Li, J. Li, C. Liu, C. Lao, Y. Fu, C. Liu, Y. Li, P. Wang, Y. He, *J. Eur. Ceram. Soc.* **2019**, *39*, 661.
[8] E. Peng, D. Zhang, J. Ding, *Adv. Mater.* **2018**, *30*, 1802404.
[9] E. Feilden, C. Ferraro, Q. Zhang, E. Garcia-Tunon, E. D'Elia, F. Giuliani, L. Vandeperre, E. Saiz, *Sci. Rep.* **2017**, *7*, 13759.
[10] J. M. Pappas, E. C. Kinzel, X. Dong, *Manuf. Lett.* **2020**, *24*, 92.
[11] I. K. Jones, Z. M. Seeley, N. J. Cherepy, E. B. Duoss, S. A. Payne, *Opt. Mater.* **2018**, *75*, 19.
[12] G. Zhang, D. Carloni, Y. Wu, *Ceram. Int.* **2020**, *46*, 17130.
[13] Z. Seeley, T. Yee, N. Cherepy, A. Drobshoff, O. Herrera, R. Ryerson, S. A. Payne, *Opt. Mater.* **2020**, *107*, 110121.
[14] S. Hu, Y. Liu, Y. Zhang, Z. Xue, Z. Wang, G. Zhou, C. Lu, H. Li, S. Wang, *J. Eur. Ceram. Soc.* **2019**, *39*, 2731.
[15] J. Hostaša, M. Schwentenwein, G. Toci, L. Esposito, D. Brouczek, A. Piancastelli, A. Pirri, B. Patrizi, M. Vannini, V. Biasini, *Scr. Mater.* **2020**, *187*, 194.
[16] F. Kotz, K. Arnold, W. Bauer, D. Schild, N. Keller, K. Sachsenheimer, T. M. Nargang, C. Richter, D. Helmer, B. E. Rapp, *Nature* **2017**, *544*, 337.
[17] D. Carloni, G. Zhang, Y. Wu, *J. Eur. Ceram. Soc.* **2021**, *41*, 781.
[18] P. Biswas, S. Mamatha, S. Naskar, Y. S. Rao, R. Johnson, G. Padmanabham, *J. Alloys Compd.* **2019**, *770*, 419.
[19] A. Goldstein, A. Krell, A. Kleebe, *J. Am. Ceram. Soc.* **2016**, *99*, 3173.
[20] S. F. Wang, J. Zhang, D. W. Luo, F. Gu, D. Y. Tang, Z. L. Dong, G. E. B. Tan, W. X. Que, T. S. Zhang, S. Li, L. B. Kong, *Prog. Solid State Chem.* **2013**, *41*, 20.
[21] D. G. Moore, L. Barbera, K. Masania, A. R. Studart, *Nat. Mater.* **2020**, *19*, 212.
[22] R. Johnson, P. Biswas, P. Ramavath, R. S. Kumar, G. Padmanabham, *J. Indian Ceram. Soc.* **2012**, *71*, 73.
[23] E. D. Palik, *Handbook of Optical Constants of Solids II*, Elsevier, Amsterdam, The Netherlands **1991**.
[24] A. Camposeo, L. Persano, M. Farsari, D. Pisignano, *Adv. Opt. Mater.* **2019**, *7*, 1800419.
[25] D. J. Morris, A. M. Vodnick, R. F. Cook, *Int. J. Fracture* **2005**, *136*, 265.
[26] F. Alisafaei, C.-S. Han, *Adv. Condens. Matter Phys.* **2015**, *2015*, 391579.
[27] J. Klein, M. Stern, G. Franchin, M. Kayser, C. Inamura, S. Dave, J. C. Weaver, P. Houk, P. Colombo, M. Yang, N. Oxman, *3D Print. Addit. Manuf.* **2015**, *2*, 92.
[28] N. A. Dudukovic, L. L. Wong, D. T. Nguyen, J. F. Destino, T. D. Yee, F. J. Ryerson, T. Suratwala, E. B. Duoss, R. Dylla-Spears, *ACS Appl. Nano Mater.* **2018**, *1*, 4038.
[29] I. Cooperstein, E. Shukrun, O. Press, A. Kamyshny, S. Magdassi, *ACS Appl. Mater. Interfaces* **2018**, *10*, 18879.
[30] K. Sasan, A. Lange, T. D. Yee, N. Dudukovic, D. T. Nguyen, M. A. Johnson, O. D. Herrera, J. H. Yoo, A. M. Sawvel, M. E. Ellis, C. M. Mah, R. Ryerson, L. L. Wong, T. Suratwala, J. F. Destino, R. Dylla-Spears, *ACS Appl. Mater. Interfaces* **2020**, *12*, 6736.
[31] D. T. Nguyen, C. Meyers, T. D. Yee, N. A. Dudukovic, J. F. Destino, C. Zhu, E. B. Duoss, T. F. Baumann, T. Suratwala, J. E. Smay, R. Dylla-Spears, *Adv. Mater.* **2017**, *29*, 1701181.
[32] C. Liu, B. Qian, R. Ni, X. Liu, J. Qiu, *RSC Adv.* **2018**, *8*, 31564.
[33] J. F. Destino, N. A. Dudukovic, M. A. Johnson, D. T. Nguyen, T. D. Yee, G. C. Egan, A. M. Sawvel, W. A. Steele, T. F. Baumann, E. B. Duoss, T. Suratwala, R. Dylla-Spears, *Adv. Mater. Technol.* **2018**, *3*, 1700323.
[34] K. Takanabe, *ACS Catal.* **2017**, *7*, 8006.
[35] T. J. Whittemore, C. Xue, J. Huang, J. C. Gallucci, C. Turro, *Nat. Chem.* **2020**, *12*, 180.
[36] S. K. Loeb, P. J. J. Alvarez, J. A. Brame, E. L. Cates, W. Choi, J. Crittenden, D. D. Dionysiou, Q. Lin. G. Li-puma, X. Quan, D. L. Sedlak, T. D. Waite, P. Westerhoff, J. H. Kim, *Environ. Sci. Technol.* **2019**, *53*, 2937.
[37] Y. Zhao, L. Zheng, R. Shi, S. Zhang, X. Bian, F. Wu, X. Cao, G. I. N. Waterhouse, T. Zhang, *Adv. Energy Mater.* **2020**, *10*, 2002199.
[38] P. Zhang, X. W. Lou, *Adv. Mater.* **2019**, *31*, 1900281.
[39] M. Q. Wang, J. Yan, H. P. Cui, S. G. Du, *Mater. Charact.* **2013**, *76*, 39.
[40] M. H. Ahmed, T. E. Keyes, J. A. Byrne, C. W. Blackledge, J. W. Hamilton, *J. Photochem. Photobiol., A* **2011**, *222*, 123.
[41] X. D. Wang, F. Shi, W. Huang, C. M. Fan, *Thin Solid Films* **2012**, *520*, 2488.
[42] Y. Li, X. Zhou, W. Chen, L. Li, M. Zen, S. Qin, S. Sun, *J. Hazard. Mater.* **2012**, *25*, 227.
[43] M. Khatamian, S. Hashemian, A. Yavari, M. Saket, *Mater. Sci. Eng., B* **2012**, *177*, 1623.
[44] Y. Zhang, J. C. Crittenden, D. W. Hand, D. L. Perram, *Environ. Sci. Technol.* **1994**, *28*, 435.
[45] J. G. Yu, X. J. Zhao, Q. N. Zhao, *Mater. Chem. Phys.* **2001**, *69*, 25.